Research Square

Preprints are preliminary reports that have not undergone peer review.
They should not be considered conclusive, used to inform clinical practice,
or referenced by the media as validated information.

Harmonic Phase Relationships and Ultrafast Response of Plasmonic Nanoantennas: Implications for Quantum Information Applications

Hüseyin U. Tepe

huseyin.tepe1992@gmail.com

Independent Researcher

Research Article

Keywords:

Posted Date: November 27th, 2026

DOI: https://doi.org/10.21203/rs.3.rs-11680800/v1

License: This work is licensed under a Creative Commons Attribution 4.0 International License.
Read Full License

Additional Declarations: No competing interests reported.

Harmonic Phase Relationships and Ultrafast Response of Plasmonic Nanoantennas: Implications for Quantum Information Applications

Hüseyin Umut Tepe[1*]

[1]Independent Researcher, Halmstad, 30248, Sweden.

Corresponding author. E-mail: huseyin.tepe1992@gmail.com;

Abstract

Plasmonic nanoantennas offer strongly localized electromagnetic fields and enhanced nonlinear optical responses, making them interesting candidates for future ultrafast optical and quantum information applications. However, their potential use in such applications depends not only on field enhancement but also on the spatial stability of phase relationships and the time-dependent response of the induced fields. Here, these properties are investigated using a nonlinear hydrodynamic model of a gold nanoantenna optimized for excitation at a typical telecom wavelength. Spatial phase maps of the fundamental, second- and third-harmonic fields reveal piecewise-constant relative phase relationships across the simulated domain. The time-dependent response is further examined under few-cycle excitation using a 10 fs incident pulse. No clear trailing ring-down response is observed in the calculated harmonic waveforms. These results demonstrate spatially structured phase relationships and a rapid nonlinear response in the simulated nanoantenna, that may be relevant to future ultrafast optical and quantum information technologies.

Keywords: Plasmonic nanoantennas, nonlinear plasmonics, hydrodynamic modeling, ultrafast plasmonics, harmonic generation, second-harmonic generation, third-harmonic generation, nonlinear phase relationships, near-field optics

1 Introduction

Quantum computing is an emerging technology with potential applications in cryptography, quantum chemistry and the simulation of physical systems[1, 2].

The core conceptual difference between classical and quantum computing lies in how information is represented and manipulated (bits versus qubits). In classical computers, a bit has a definite value of either 0 or 1. A quantum bit, or qubit, can instead exist in a superposition of the two basis states, denoted as $|0\rangle$ and $|1\rangle$. A general qubit state can be expressed as

$$|\psi\rangle = \alpha|0\rangle + \beta|1\rangle$$

where α and β are complex probability amplitudes satisfying

$$|\alpha|^2 + |\beta|^2 = 1$$

Quantum gates manipulate qubits and can create or modify correlations between them, including quantum entanglement. While a system of N classical bits has one definite configuration at a time, a general pure state of N qubits requires 2^N complex probability amplitudes. This exponential growth makes the classical computation of quantum systems computationally demanding.

A quantum state can be expressed as $|\psi\rangle = \sum \alpha_i|\psi_i\rangle$, where α_i are the probability amplitudes and ψ_i are the basis states. As an example, our face can be represented by a series of spherical harmonics $F = \sum a_{\ell m} Y_{\ell m}$, in a manner analogous to a Fourier series. A similar representation is used to describe quantum states, where the coefficients are probability amplitudes. Each basis function contributes to the overall representation, meaning that changing one coefficient can alter the global structure rather than just a single point or pixel. While representing a face is merely a mathematical example, simulating the evolution of a complex quantum system, such as a molecule undergoing a chemical reaction, is a much more interesting.

A central challenge in quantum computing is decoherence, but what does it mean? Consider a simplified example in which your two interests are playing chess and reading books. Your state can be represented as

$$|\psi\rangle = \alpha|C\rangle + \beta|B\rangle$$

where C and B denote chess and reading a book, respectively. Imagine that you have two friends: the first only plays chess, while the second only reads books. When you meet your first friend, you play chess together, and when you meet your second friend, you read books. The combined state of you and your friend can then be written as:

$$|\Psi\rangle = \alpha|C\rangle|F_{chess}\rangle + \beta|B\rangle|F_{book}\rangle$$

The activity is now correlated with the state of your friend. In this example, the combined state is entangled because the state of each system cannot be described independently of the other. If, instead, you were to play chess or read books independently of which friend you spend time with, there would be no entanglement, and the combined state could be written as

$$|\Psi\rangle = (\alpha|C\rangle + \beta|B\rangle)|F_0\rangle$$

Now, consider replacing the two friends with a single surrounding system, or environment, that can become correlated with your activity. Let its corresponding states be

$|S_{chess}\rangle$ and $|S_{book}\rangle$. If these states are distinguishable and orthogonal, such that

$$\langle S_{chess}|S_{book}\rangle = 0$$

the environment can distinguish between the two alternatives. Although the combined system may still retain its quantum coherence, interference between the alternatives becomes inaccessible when observing your state alone. This loss of observable coherence is known as decoherence (a more detailed explanation is provided in Appendix A).

Photons, in contrast, interact only weakly with each other under ordinary conditions and can maintain their coherence over relatively long propagation distances. However, their weak direct interactions also limit the ability to manipulate photons, which is important for certain quantum operations[3]. Nonlinear optical materials allow for interactions between light fields. At high excitation intensities, nonlinear optical responses can become significant, even in materials that exhibit weak nonlinearities such as air. These responses can generate new optical frequencies, for example through second- and third-harmonic generation. Consequently, developing materials and structures that produce substantial nonlinear responses at relatively low excitation intensities is of interest.

Plasmonic structures is a interesting option to nanoscale photonic systems. Quantum plasmonics is a field investigating the interaction between quantum states of light and collective electron excitations in metallic nanostructures, offering possibilities for enhanced light-matter interactions and nanoscale quantum devices [4]. Metallic nanoantennas are structures that typically range from tens to a few thousand nanometers in size and are designed to resonate at specific optical frequencies. A properly designed nanoantenna can concentrate incident light into nanoscale regions, producing strong local electric fields that can enhance the nonlinear optical response of the material [5]. Although metallic nanoantennas can exhibit strong nonlinear responses relative to their small interaction volumes[6–8], achieving substantial nonlinear frequency conversion can still require impractically high incident intensities. Improving the conversion efficiency and reducing the required excitation intensity therefore remain important research objectives [9].

Furthermore, a metallic nanoantenna is not purely photonic, as the incident electromagnetic field drives the collective motion of conduction electrons. This electron motion generates an induced electromagnetic response through radiation and absorption. Metallic nanoantennas are also subject to dephasing processes that affect the collective electron oscillations. In particular, interactions with other modes and the surrounding environment can influence the phase relationships between different excitations.

For example, multiresonant nanoantennas can support multiple modes through appropriately designed geometries. Intense illumination may also excite higher-order modes, while interactions with nearby nanoantennas, particles, or molecules can introduce additional coupling mechanisms. The dephasing time of collective electron resonances in metallic nanostructures has been reported to be on the order of several to tens of femtoseconds. Furthermore, shorter excitation pulses have broader spectral

bandwidths and can therefore overlap with multiple resonances, potentially allowing several modes to be excited simultaneously.

Despite these limitations, metallic nanoantennas offer unique advantages, including the ability to miniaturize optical components and relax phase-matching requirements compared with conventional bulk nonlinear optical crystals.

An interesting connection between higher-order optical modes and quantum-state representations was recently explored in a hydrodynamic simulation study of sharp-tipped gold nanorods. Under intense illumination, spatial modes resembling spherical harmonics, ($Y_{\ell m}$), were observed near the antenna tips [10]. Spherical harmonics form an orthogonal basis, satisfying

$$\langle Y_{\ell m} | Y_{\ell' m'} \rangle = \delta_{\ell \ell'} \delta_{m m'},$$

and can therefore be used to represent complex states as combinations of distinct modes. Although spherical harmonics are not exclusive to quantum mechanics, their mathematical properties provide an interesting connection to the basis representations used in quantum-state descriptions. This raises questions regarding the phase relationships between higher-order modes and their temporal evolution under intense optical excitation.

The purpose of the present study is to investigate the phase relationships between higher-order modes and the ultrafast electron dynamics responsible for the nonlinear optical response of metallic nanoantennas. A hydrodynamic model is employed to simulate the collective motion of free electrons in a gold nanoantenna with a sharp metal-vacuum interface, which provides a macroscopic model for the collective electron dynamics while retaining the microscopic effects of the electron gas [11, 12].

The study aims to improve the understanding of how higher-order modes emerge and interact during intense optical excitation, providing further insight into the potential of metallic nanoantennas for controlling nonlinear optical responses at the nanoscale.

2 Results

2.1 Phase Maps

Assuming that the incident electric field has the complex amplitude $E_1 e^{i(\phi_1 + \Delta)}$, the corresponding second- and third-harmonic amplitudes in a nonlinear medium can be expressed as

$$E_{2\omega} \propto \chi^{(2)} E_1^2$$

and

$$E_{3\omega} \propto \chi^{(3)} E_1^3,$$

respectively. Here, Δ represents an additional phase shift applied to the incident field. Since the nonlinear response scales with the corresponding integer power of the incident field, the phase shift is multiplied by the harmonic order. Consequently, the phase differences

$$\Delta\phi_2 = \phi_{2\omega} - 2\phi_\omega,$$
$$\Delta\phi_3 = \phi_{3\omega} - 3\phi_\omega,$$

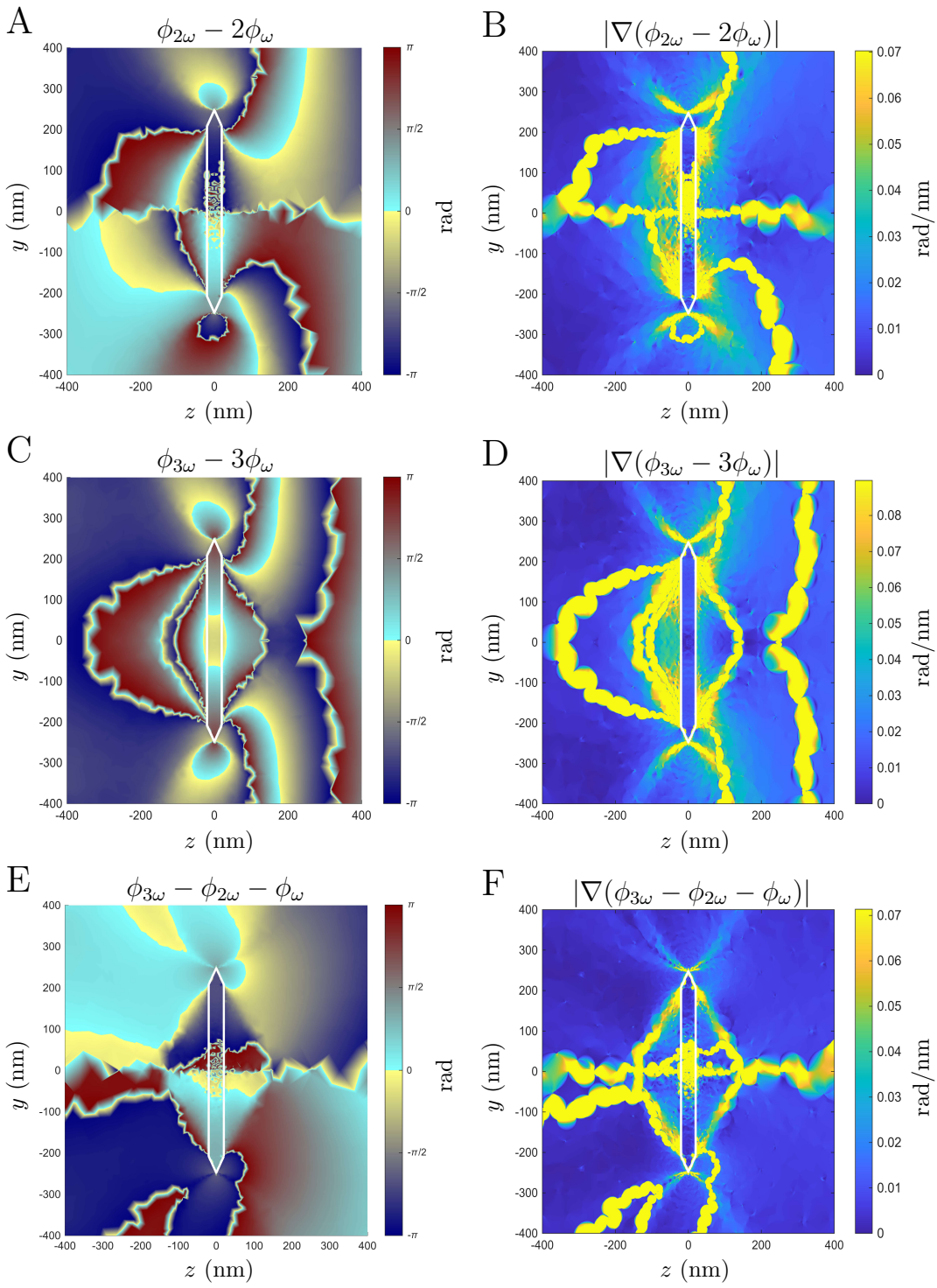

Fig. 1: (A), (C) and (E) show the phase-difference maps for second-harmonic generation, third-harmonic generation and the combined third-/second-/fundamental-frequency relationship, respectively. The phase differences are spatially piecewise constant, with non-zero offsets in some regions. (B), (D) and (F) show the corresponding phase-gradient magnitudes, indicating the spatial variation of the relative phase. Regions with small phase gradients are potentially suitable for experimental probing, as small probe-position variations are less likely to introduce significant phase changes. The most favourable probe position is approximately 30 nm above the antenna tip, within a region extending roughly 20 nm along each spatial direction, where the nonlinear signal is strong and the phase gradients are small.

and

$$\Delta\phi_{321} = \phi_{3\omega} - \phi_{2\omega} - \phi_{\omega}$$

are independent of the applied input phase shift Δ. Figures 1a, 1c, and 1e show that these phase differences are spatially piecewise constant, indicating that the relative phase relationships are maintained within regions of the simulated domain. For experimental applications, the most suitable regions are expected to be those combining strong nonlinear signal amplitudes with small spatial variations in the relative phase.

The previous study [10] showed that the strongest fields are concentrated near the antenna tips. Figures 1b, 1d and 1f show regions with nearly zero phase-gradient magnitude, extending over an approximately 20 nm radius around a position located about 30 nm above the antenna tips. These regions are of particular interest for potential experimental probing, as they combine relatively stable phase relationships with strong nonlinear fields.

The sensitivity of the phase maps to changes in the input field amplitude, phase and wavelength was also investigated. The corresponding results are presented in Figures B1, B2, and B3 and B4. Reducing the input field amplitude by one order of magnitude produced no noticeable changes in the phase maps. A further reduction by two orders of magnitude had little effect on the second-harmonic phase map, but introduced substantial noise into the third-harmonic phase map.

As expected, applying an additional phase shift to the incident field did not alter the calculated phase differences. The sensitivity to variations in the excitation wavelength was also investigated to assess the influence of possible laser wavelength drift. A wavelength shift of 5 nm produced no visible changes in the phase maps, suggesting that the observed phase relationships are relatively insensitive to small variations in the excitation wavelength.

2.2 Poynting Vector Maps

Figure 2 shows the instantaneous Poynting vectors associated with the fundamental, second- and third-harmonic fields. While the electric-field spectrum contains distinct fundamental and harmonic components, the corresponding power spectrum is more complicated.

The frequency components of the Poynting vector arise from products of the electric and magnetic fields. Consequently, the power spectrum contains frequency combinations that are not present as individual components in the electric-field spectrum. For example, the time-dependent Poynting vector at 6ω can receive contributions from the frequency pairs $(\omega, 5\omega)$ and $(2\omega, 4\omega)$, since both pairs sum to 6ω. This illustrates why the frequency content of the Poynting vector is more complex than that of the electric field alone.

The Poynting-vector maps, particularly near the antenna tips, show directional features in the second-harmonic response, while the third-harmonic response exhibits a combination of conservative and radiative characteristics. The mean far-field electric-field amplitudes and the calculated outward power flows are summarized in Table 1. The DC contributions arise from equal-frequency field pairs, such as $(2\omega, 2\omega)$ and $(3\omega, 3\omega)$, which produce time-averaged Poynting vectors associated with propagating power. In contrast, unequal-frequency pairs, such as $(1\omega, 5\omega)$ contributing to $P(6\omega)$,

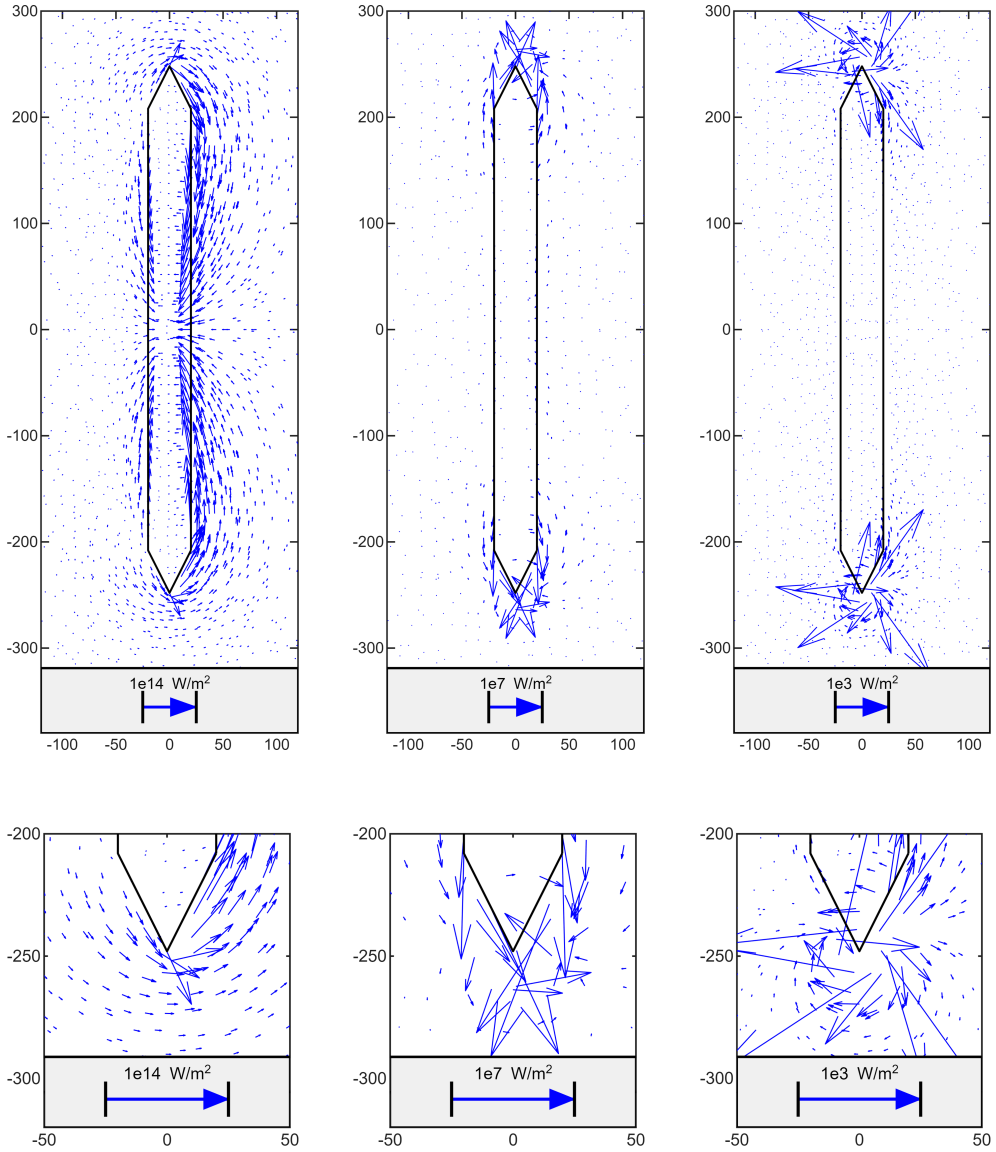

Fig. 2: Spatial distributions of the Poynting vector for the fundamental ω, second-harmonic 2ω, and third-harmonic 3ω components. The vector fields illustrate the direction and spatial distribution of electromagnetic power flow around the nanoantenna.

generate AC components that oscillate in time and do not contribute to the time-averaged propagating power flow.

For a non-magnetic medium, the power associated with a normally propagating field can be estimated from

$$P = \frac{A|E|^2}{2Z_0},$$

where A is the observation area and $Z_0 \simeq 377\ \Omega$ is the impedance of free space. Using the mean normal electric-field amplitudes, the estimated SHG and THG outward powers are 2.33×10^{-18} W and 9.9×10^{-25} W, respectively. These estimates are of the same order of magnitude as the corresponding simulated DC power values.

Table 1: Electric-field amplitudes and outward power at the observation surface, distanced 700 nm away from the nanoantenna. The DC and AC powers are given by the time-averaged $\langle \mathbf{P} \rangle = \mathbf{E} \times \mathbf{H}^*$ and the instantaneous $\mathbf{P}(n\omega) = FFT\{\mathbf{E}(t, \mathbf{x})\}_{n\omega} \times FFT\{\mathbf{H}(t, \mathbf{x})\}_{n\omega}$, respectively.

Harmonic	Mean normal (V m^{-1})	Mean tangential (V m^{-1})	Outward power (W)	
			DC	AC
1ω	2.74×10^{4}	5.52×10^{4}	2.51×10^{-5}	-
2ω	1.69×10^{-2}	3.28×10^{-2}	4.81×10^{-18}	5.75×10^{-14}
3ω	1.10×10^{-5}	3.19×10^{-5}	1.26×10^{-24}	1.57×10^{-17}

2.3 Short Pulse Excitation

In conventional nanoantenna experiments, longer excitation pulses are often used to increase the amplitude of the induced oscillations. However, longer excitation durations may be disadvantageous for applications involving quantum information, where dephasing can limit the time available for coherent operations. Efficient excitation of a nanoantenna generally requires spectral overlap between the incident pulse and the antenna resonance. Longer pulses have narrower spectral bandwidths and can therefore provide more efficient excitation when their central frequency is well matched to the resonance. Shorter pulses, in contrast, have broader spectral bandwidths. Although their peak spectral intensity may be lower, their broader bandwidth can allow them to excite multiple resonances, including modes that are spectrally separated from the central frequency of the incident pulse.

The nonlinear hydrodynamic simulations in the previous study [10] showed that the temporal profile of the absorbed fundamental field closely follows that of the incident pulse, with no noticeable trailing response. The second- and third-harmonic fields also exhibited pulse durations consistent with the expected scaling for harmonic generation. This behaviour indicates that the simulated nonlinear response follows the excitation on a very short timescale, making the system suitable for numerical

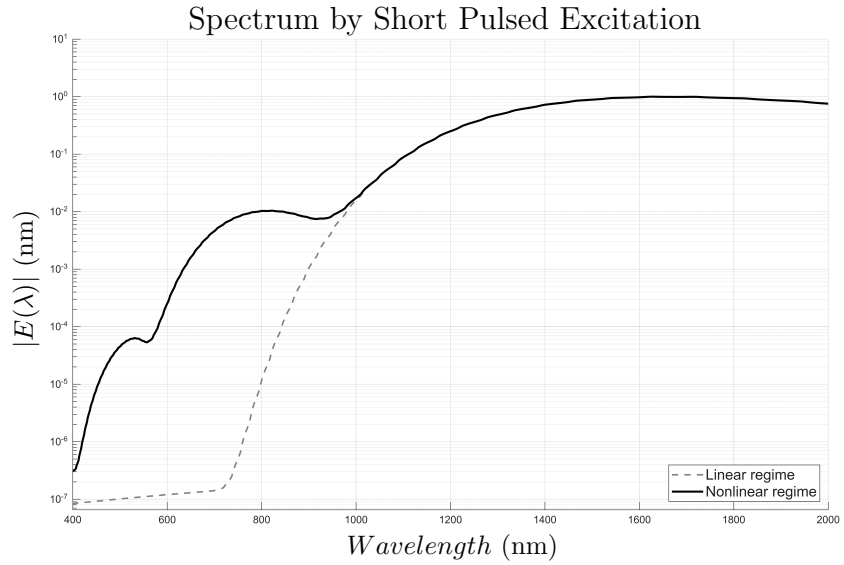

Fig. 3: Normalized spectral electric-field response of the nanoantenna under short-pulse excitation in the linear and nonlinear regimes. The linear response (dashed curve) is obtained using an incident field amplitude of 1 V/m, whereas the nonlinear hydrodynamic response (solid curve) is calculated using an incident field amplitude of 10^7 V/m.

investigation in the few-cycle excitation regime. Experimentally, few-cycle pulses have already been used to excite different types of subwavelength nanostructures [13–15].

The suitable pulse duration depends on both the damping properties of the metal and the resonance characteristics of the nanoantenna. For gold, the damping parameter used in the simulations is $\gamma = 1.075 \times 10^{14}$ s^{-1}, corresponding to a characteristic timescale of $1/\gamma \approx 9.3$ fs. This timescale provides an indication of the damping of the induced electronic response, rather than a direct measure of the coherence time of a quantum state. The antenna investigated here is optimized for a resonance at 1560 nm, corresponding to an optical cycle duration of approximately 5.2 fs. Although pulses shorter than one optical cycle can be used, they contain less energy within the resonant spectral range and may therefore produce a weaker resonant oscillation.

The temporal response also depends on the antenna configuration. Individual nanoparticles and isolated nanoantennas generally exhibit lower quality factors and shorter ring-up times, allowing them to respond more rapidly to an incident pulse [16, 17]. In contrast, collective resonances in coupled nanoantenna arrays can have higher quality factors and longer ring-up times [16–18].For applications requiring rapid nonlinear optical responses, single or paired nanoantennas may therefore be preferable because of their potentially shorter response times, compact dimensions and reduced phase-matching requirements.

Figure 3 compares the normalized spectral emission of the linear and nonlinear responses, obtained using excitation-field amplitudes of 1 and 10^7 V/m, respectively.

The approximate pulse durations estimated from the spectral peaks are 7.5, 5.8 and 4.7 fs for the fundamental, second- and third-harmonic components, respectively. For ideal harmonic generation, the pulse duration is expected to scale approximately as $1/\sqrt{n}$, where n is the harmonic order. Although the spectral overlap makes accurate pulse-duration estimation difficult, the estimated values appear to follow this scaling behaviour.

3 Methods

The phase maps are obtained by evaluating the following expressions:

$$\Delta\phi_2(\mathbf{x}) = \arg\left[F_2(\mathbf{x})(F_1^*(\mathbf{x}))^2\right], \tag{1}$$

$$\Delta\phi_3(\mathbf{x}) = \arg\left[F_3(\mathbf{x})(F_1^*(\mathbf{x}))^3\right], \tag{2}$$

$$\Delta\phi_{321}(\mathbf{x}) = \arg\left[F_3(\mathbf{x})F_2^*(\mathbf{x})F_1^*(\mathbf{x})\right], \tag{3}$$

where $F_n(\mathbf{x})$ denotes the Fourier component of the y-component of the electric field, $E_y(\mathbf{x}, t)$, evaluated at the frequency $\omega = n\omega_1$. The Fourier components can be expressed in terms of their amplitudes and phases as

$$F_n(\mathbf{x}) = |F_n(\mathbf{x})|e^{i\phi_n(\mathbf{x})}. \tag{4}$$

For example, the complex conjugate of the fundamental component is

$$F_1^*(\mathbf{x}) = |F_1(\mathbf{x})|e^{-i\phi_1(\mathbf{x})}. \tag{5}$$

Consequently,

$$F_2(F_1^*)^2 = |F_2||F_1|^2 e^{i(\phi_2 - 2\phi_1)}, \tag{6}$$

and its argument gives the second-harmonic phase difference,

$$\Delta\phi_2 = \phi_2 - 2\phi_1. \tag{7}$$

The Poynting-vector maps were obtained by performing a fast Fourier transform (FFT) of the electric ($\mathbf{E}$) and magnetic ($\mathbf{H}$) fields on the yz-plane. The z-axis is parallel to the propagation direction of the incident light, while the y-axis is parallel to the excitation polarization. The relevant Fourier components were then selected to calculate the corresponding Poynting-vector contributions. The AC and DC outward power flows are both reported in Table 1. The time-independent DC contribution is calculated using

$$\langle \mathbf{P}_{n\omega_1}(\mathbf{x}) \rangle = \mathbf{E}_{n\omega_1}(\mathbf{x}) \times \mathbf{H}^*_{n\omega_1}(\mathbf{x}), \tag{8}$$

whereas the corresponding AC contribution is calculated without taking the complex conjugate of the magnetic-field component.

The hydrodynamic model is described by the following system of coupled equations:

$$\nabla \times (\nabla \times \mathbf{E}) + \partial_{tt}\mathbf{E}/c^2 + \mu_0 \partial_{tt}\mathbf{P} = 0 \tag{9a}$$

$$m_e n(\partial_t \mathbf{v} + (\mathbf{v}\cdot\nabla)\mathbf{v} + \gamma\mathbf{v}) = -en(\mathbf{E} + \mathbf{v}\times\mathbf{H}) - \vec{\nabla}p \tag{9b}$$

$$p = \frac{\hbar^2(3\pi^2)^{3/2}}{5m_e} n^{5/3} \tag{9c}$$

$$\partial_t n + \nabla\cdot(n\mathbf{v}) = 0 \tag{9d}$$

$$\partial_t \mathbf{P} = -en\mathbf{v} \tag{9e}$$

$$\tag{9f}$$

Here, c is the speed of light, m_e is the electron mass, n is the electron number density, $\mathbf{v}$ is the electron-fluid velocity, $\mathbf{P}$ is the polarization density, and γ is the damping parameter. For gold, the damping parameter is set to $\gamma_{\mathrm{Au}} = 1.075 \times 10^{14}$ s^{-1}. The pressure term p describes the quantum pressure of the electron gas, modelled using the Fermi-gas expression in Equation 9c. Further details regarding the numerical implementation and simulation parameters are provided in the previous study [10].

Few-cycle pulse excitation produces a spectrum with overlapping peaks, which complicates the estimation of the individual pulse durations. To estimate these durations, three Gaussian functions centred at 1560, 780 and 520 nm are fitted to the spectral peaks in Figure 3. The full width at half maximum (FWHM) of each fitted Gaussian is then used to estimate the corresponding pulse duration [10]

ChatGPT (OpenAI) was used during manuscript preparation to assist with the development and clarification of theoretical background concerning quantum mechanics, and language editing. The numerical simulations, methodology, scientific interpretation of the results, and conclusions are the author's own work. The author has reviewed and verified all AI-assisted content and takes full responsibility for the accuracy and integrity of the manuscript.

4 Conclusion

The phase maps show that the fundamental, second- and third-harmonic fields have spatially piecewise-constant phase relationships throughout the simulated yz-plane. The Poynting-vector maps complement this analysis by illustrating the spatial distribution and direction of the associated power flows. Together, these results identify regions approximately 20 nm above the antenna tips where probes or auxiliary molecules, particles or tips could potentially be positioned to interact with the localized fields.

In quantum information applications, preserving coherence is important, and the time-dependent behaviour of the optical system therefore deserves attention. The high damping rate of gold motivates the use of short excitation pulses and rapid optical responses. In this study, a 10 fs incident pulse was used to excite a single gold nanoantenna. The estimated pulse durations of the second- and third-harmonic components show no clear evidence of a trailing ring-down response. This suggests that the simulated nanoantenna exhibits a very rapid nonlinear response, which may be of

interest for future applications in ultrafast nonlinear optics and quantum information technologies.

The hydrodynamic model describes the collective motion of conduction electrons within the gold nanoantenna, subject to a hard-wall boundary condition. Microscopic electron spill-out at the surface is not resolved. This limitation may affect the localized surface-plasmon response and represents an important direction for future studies.

Declarations

- I have received no funding.
- The author declare no competing interests.
- All contributions belong to the corresponding author "Hüseyin U. Tepe".

Appendix A Decoherence

The entangled friend state and its conjugate transpose are

$$|\Psi\rangle = a|C\rangle|F_C\rangle + be^{i\phi}|B\rangle|F_B\rangle, \tag{A1}$$

and

$$\langle\Psi| = a^*\langle C|\langle F_C| + b^*e^{-i\phi}\langle B|\langle F_B|. \tag{A2}$$

Here, a and b are complex probability amplitudes, ϕ is the relative phase, and the normalization condition is

$$|a|^2 + |b|^2 = 1. \tag{A3}$$

Assuming orthonormal states for both subsystems, the four possible combined basis states are

$$\begin{aligned} |1\rangle &= |C, F_C\rangle, \\ |2\rangle &= |C, F_B\rangle, \\ |3\rangle &= |B, F_C\rangle, \\ |4\rangle &= |B, F_B\rangle. \end{aligned} \tag{A4}$$

In this basis, the combined state vector becomes

$$|\Psi\rangle = \begin{pmatrix} a \\ 0 \\ 0 \\ be^{i\phi} \end{pmatrix}. \tag{A5}$$

The full density operator is defined as

$$\rho_{SF} = |\Psi\rangle\langle\Psi|. \tag{A6}$$

Expanding the outer product gives

$$\rho_{SF} = \begin{pmatrix} |a|^2 & 0\ 0 & ab^* e^{-i\phi} \\ 0 & 0\ 0 & 0 \\ 0 & 0\ 0 & 0 \\ a^* b e^{i\phi} & 0\ 0 & |b|^2 \end{pmatrix}. \tag{A7}$$

The off-diagonal elements contain the relative phase information. Consequently, the phase information is not lost in the combined system.

For example, it can be accessed through measurements in the following superposition basis:

$$|\Phi^+\rangle = \frac{|C, F_C\rangle + |B, F_B\rangle}{\sqrt{2}}, \tag{A8}$$

$$|\Phi^-\rangle = \frac{|C, F_C\rangle - |B, F_B\rangle}{\sqrt{2}}. \tag{A9}$$

The corresponding measurement probabilities are

$$P(\Phi^\pm) = |\langle \Phi^\pm | \Psi \rangle|^2 = \frac{1}{2} \left| a \pm b e^{i\phi} \right|^2. \tag{A10}$$

These probabilities depend on the relative phase, demonstrating that the phase information remains accessible through joint measurements of the combined system.

However, if we consider measurements on the original system alone, the friend or surrounding environment must be traced out. The resulting reduced density operator is

$$\rho_S = \mathrm{Tr}_F(\rho_{SF}). \tag{A11}$$

Expanding the partial trace gives

$$\begin{aligned} \rho_S = |a|^2 |C\rangle\langle C| \langle F_C | F_C \rangle \\ + a b^* e^{-i\phi} |C\rangle\langle B| \langle F_B | F_C \rangle \\ + a^* b e^{i\phi} |B\rangle\langle C| \langle F_C | F_B \rangle \\ + |b|^2 |B\rangle\langle B| \langle F_B | F_B \rangle. \end{aligned} \tag{A12}$$

If the environmental states are normalized and orthogonal,

$$\langle F_C | F_C \rangle = \langle F_B | F_B \rangle = 1, \tag{A13}$$

and

$$\langle F_C | F_B \rangle = \langle F_B | F_C \rangle = 0, \tag{A14}$$

the off-diagonal terms vanish, leaving

$$\boxed{\rho_S = |a|^2 |C\rangle\langle C| + |b|^2 |B\rangle\langle B|.} \tag{A15}$$

The relative phase is therefore no longer accessible through measurements of the original system alone. This is known as decoherence. Importantly, the phase information has not been destroyed in the combined system; rather, it has become inaccessible when the environmental degrees of freedom are ignored.

Appendix B Extra Phase Maps

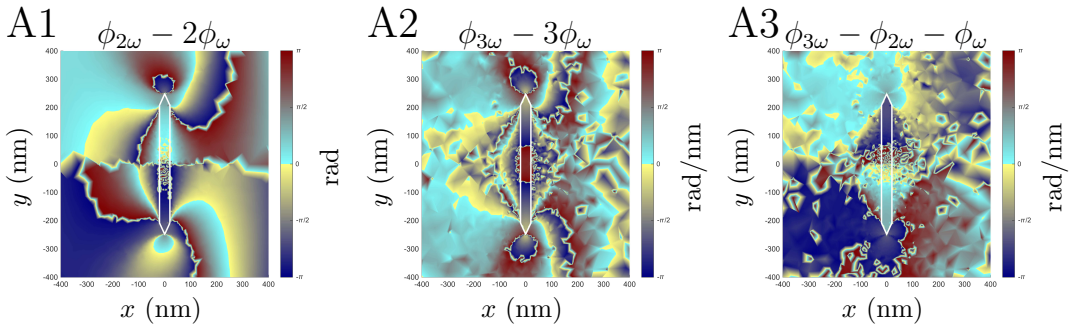

(a)

Fig. B1: Spatial distributions of the nonlinear phase differences for a reduced incident electric-field amplitude of 10^5V/m. The panels show (left to right) $\phi_{2\omega} - 2\phi_\omega$, $\phi_{3\omega} - 3\phi_\omega$, and $\phi_{3\omega} - \phi_{2\omega} - \phi_\omega$.

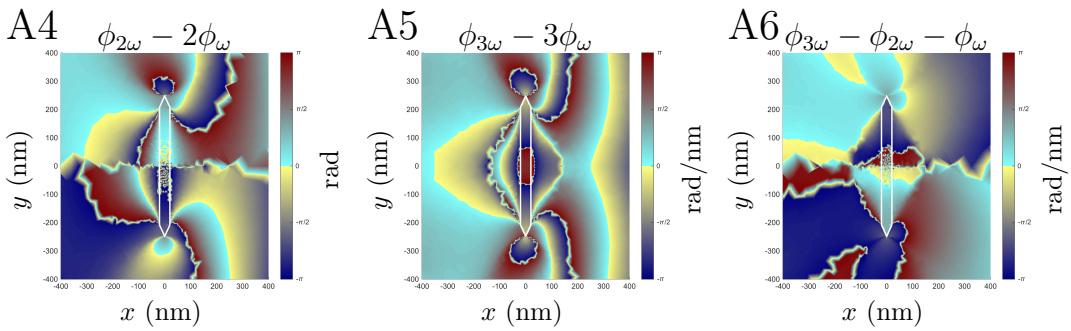

Fig. B2: Spatial distributions of the nonlinear phase differences when the incident pulse phase is shifted by 90° relative to the reference excitation. The panels show (left to right) $\phi_{2\omega} - 2\phi_\omega$, $\phi_{3\omega} - 3\phi_\omega$, and $(\phi_{3\omega} - \phi_{2\omega} - \phi_\omega$.

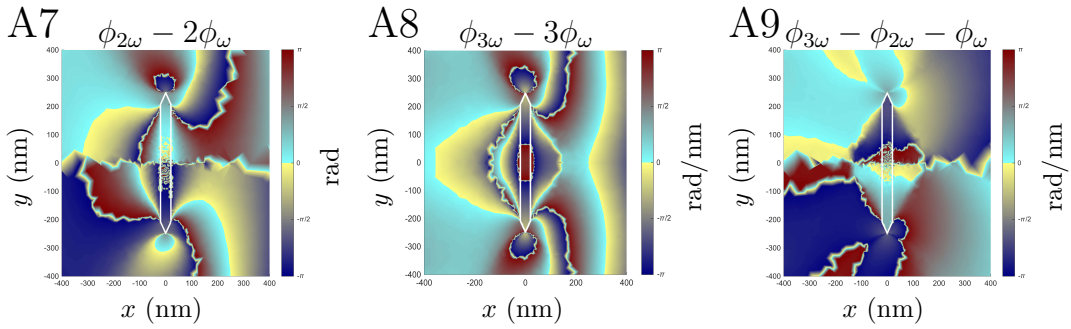

Fig. B3: Spatial distributions of the nonlinear phase differences for an incident wavelength of 1555 nm. The panels show (left to right) $\phi_{2\omega} - 2\phi_\omega$, $\phi_{3\omega} - 3\phi_\omega$, and $\phi_{3\omega} - \phi_{2\omega} - \phi_\omega$.

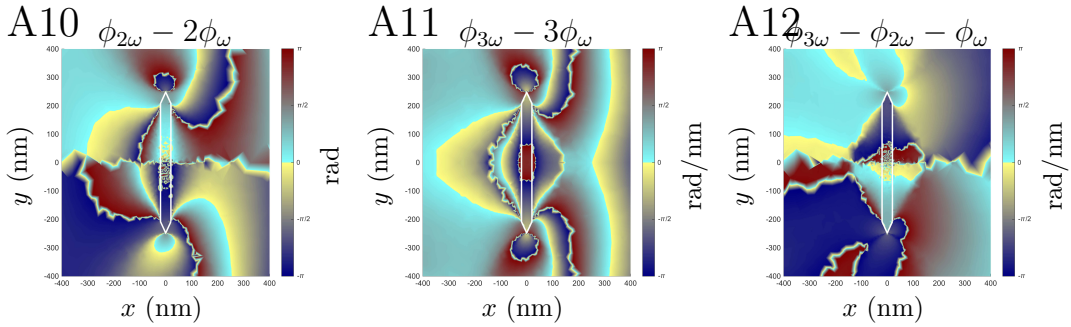

Fig. B4: Spatial distributions of the nonlinear phase differences for an incident wavelength of 1565 nm. The panels show (left to right) $(\phi_{2\omega} - 2\phi_\omega)$, $(\phi_{3\omega} - 3\phi_\omega)$, and $(\phi_{3\omega} - \phi_{2\omega} - \phi_\omega)$. The bottom row shows magnified views of the lower nanorod tips.

References

[1] Wang, J., Sciarrino, F., Laing, A., Thompson, M.G.: Integrated photonic quantum technologies. Nature Photonics **14**, 273–284 (2020) https://doi.org/10.1038/s41566-019-0532-1

[2] Feynman, R.P.: Simulating physics with computers. International Journal of Theoretical Physics **21**, 467–488 (1982) https://doi.org/10.1007/BF02650179

[3] Chang, D.E., Vuletić, V., Lukin, M.D.: Quantum nonlinear optics — photon by photon. Nature Photonics **8**, 685–694 (2014) https://doi.org/10.1038/nphoton.2014.192

[4] Tame, M.S., McEnery, K.R., Özdemir, Ş.K., Lee, J., Maier, S.A., Kim, M.S.: Quantum plasmonics. Nature Physics **9**, 329–340 (2013) https://doi.org/10.1038/nphys2615

[5] Tasgin, M.E.: Metal nanoparticle plasmons operating within a quantum lifetime. Nanoscale **5**(18), 8616–8624 (2013) https://doi.org/10.1039/C3NR02270F

[6] Jeong, T.-I., Oh, D.K., Kim, S., Park, J., Kim, Y., Mun, J., Kim, K., Chew, S.H.: Deterministic nanoantenna array design for stable plasmon-enhanced harmonic generation. Nanophotonics **12**(3), 619–629 (2023) https://doi.org/10.1515/nanoph-2022-0365

[7] Aouani, H., Rahmani, M., Navarro-Cia, M., Maier, S.A.: Third-harmonic-upconversion enhancement from a single semiconductor nanoparticle coupled to a plasmonic antenna. Nature Nanotechnology **9**(4), 290–294 (2014) https://doi.org/10.1038/nnano.2014.27

[8] Schraml, K., Regler, A., Bartl, J., Glashagen, J., Wierzbowski, J., Finley, J.J., Kaniber, M.: Metamorphic plasmonic nanoantennas for self-enhanced nonlinear light generation. Optica **3**(12), 1453–1459 (2016) https://doi.org/10.1364/OPTICA.3.001453

[9] Singh, S.K., Abak, M.K., Taşğın, M.E.: Enhancement of four-wave mixing via interference of multiple plasmonic conversion paths. Physical Review B **93**(3) (2016)

[10] Tepe, H.U.: The origin and properties of higher-order near- and far-field modes in plasmonic metal nano-rods. Scientific Reports **15**(1), 16761 (2025) https://doi.org/10.1038/s41598-025-00878-7

[11] Ciracì, C., Pendry, J.B., Smith, D.R.: Hydrodynamic model for plasmonics: A macroscopic approach to a microscopic problem. ChemPhysChem **14**(6), 1109–1116 (2013) https://doi.org/10.1002/cphc.201200992

[12] Raza, S., Bozhevolnyi, S.I., Wubs, M., Mortensen, N.A.: Nonlocal optical response in metallic nanostructures. Journal of Physics: Condensed Matter **27**(18), 183204 (2015) https://doi.org/10.1088/0953-8984/27/18/183204

[13] Komatsu, K., Pápa, Z., Jauk, T., Bernecker, F., Tóth, L., Lackner, F., Ernst, W.E., Ditlbacher, H., Krenn, J.R., Ossiander, M., Dombi, P., Schultze, M.: Few-cycle surface plasmon polaritons. Nano Letters **24**(8), 2637–2642 (2024) https://doi.org/10.1021/acs.nanolett.3c04991

[14] Zaiats, N., Wittenbecher, L., Sytcevich, I., Viotti, A.-L., Guo, C., Babu, C., Zhuo, X., Liz-Marzán, L.M., Dias, E.J.C., Abajo, F.J., Vogelsang, J., L'Huillier, A., Arnold, C., Mikkelsen, A.: Ultrafast near-field dynamics in silver nanowires driven by few-cycle short-wave infrared pulses. ACS Photonics **13**(8), 2248–2259 (2026) https://doi.org/10.1021/acsphotonics.6c00044

[15] Nagel, P.M., Robinson, J.S., Harteneck, B.D., Pfeifer, T., Abel, M.J., Prell, J.S., Neumark, D.M., Kaindl, R.A., Leone, S.R.: Surface plasmon assisted electron acceleration in photoemission from gold nanopillars. Chemical Physics **414**, 106–111 (2013) https://doi.org/10.1016/j.chemphys.2012.03.013

[16] Qi, X., Pérez, L.A., Alonso, M.I., Mihi, A.: High q-factor plasmonic surface lattice resonances in colloidal nanoparticle arrays. ACS Applied Materials & Interfaces **16**(1), 1259–1267 (2023) https://doi.org/10.1021/acsami.3c08617

[17] Wang, W., Ramezani, M., Väkeväinen, A.I., Törmä, P., Rivas, J.G., Odom, T.W.: The rich photonic world of plasmonic nanoparticle arrays. Materials Today **21**(3), 303–314 (2018) https://doi.org/10.1016/j.mattod.2017.09.002

[18] Le-Van, Q., Zoethout, E., Geluk, E.-J., Ramezani, M., Berghuis, M., Gómez Rivas, J.: Enhanced quality factors of surface lattice resonances in plasmonic arrays of nanoparticles. Advanced Optical Materials **7**(6), 1801451 (2019) https://doi.org/10.1002/adom.201801451